JGR Space Physics

RESEARCH ARTICLE
10.1029/2021JA029192

Key Points:

- 2-D distribution of GPS scintillation in the mid-latitude ionosphere is presented, and the relation to SuperDARN echoes is studied
- The scintillation and density irregularities are related to SED base and plume, main trough, secondary plume, and secondary trough
- Density irregularities developed across a wide range of wavelengths from tens of meters to tens of kilometers

Supporting Information:

Supporting Information may be found in the online version of this article.

Correspondence to:

Y. Nishimura,
toshi16@bu.edu

Citation:

Nishimura, Y., Mrak, S., Semeter, J. L., Coster, A. J., Jayachandran, P. T., Groves, K. M., et al. (2021). Evolution of mid-latitude density irregularities and scintillation in North America during the 7–8 September 2017 storm. *Journal of Geophysical Research: Space Physics*, *126*, e2021JA029192. https://doi.org/10.1029/2021JA029192

Received 28 JAN 2021
Accepted 4 JUN 2021

Evolution of Mid-latitude Density Irregularities and Scintillation in North America During the 7–8 September 2017 Storm

Y. Nishimura[1], S. Mrak[1], J. L. Semeter[1], A. J. Coster[2], P. T. Jayachandran[3], K. M. Groves[4], D. J. Knudsen[5], N. Nishitani[6], and J. M. Ruohoniemi[7]

[1]Department of Electrical and Computer Engineering and Center for Space Physics, Boston University, Boston, MA, USA, [2]Haystack Observatory, Massachusetts Institute of Technology, Cambridge, MA, USA, [3]Physics Department, University of New Brunswick, Fredericton, NB, Canada, [4]Institute for Scientific Research, Boston College, Chestnut Hill, MA, USA, [5]Department of Physics and Astronomy, University of Calgary, Calgary, AB, Canada, [6]Institute for Space Earth Environmental Research, Nagoya University, Nagoya, Japan, [7]Bradley Department of Electrical and Computer Engineering, Virginia Tech, Blacksburg, VA, USA

Abstract Using the University Navstar Consortium (UNAVCO) Global Positioning System (GPS) receiver network in North America, we present 2-D distributions of GPS radio signal scintillation in the mid-latitude ionosphere during the 7–8 September 2017 storm. The mid-latitude ionosphere showed a variety of density structures such as the storm enhanced density (SED) base and plume, main trough, secondary plume, and secondary trough during the storm main and early recovery phases. Enhanced phase and amplitude scintillation indices were observed at the density gradients of those structures. SuperDARN radar echoes were also enhanced at the density gradients. The collocation of the scintillation and HF radar echoes indicates that density irregularities developed across a wide range of wavelengths (tens of meters to tens of kilometers) in the mid-latitude density structures. The density gradients and irregularities were also detected by Swarm and DMSP as in-situ density structures that disturbed the GPS signals. The irregularities were a substantial fraction (~10%–50%) of the background density. The density irregularity had a power law spectrum with slope of ~ −1.8, suggesting that gradient drift instability (GDI) contributed to turbulence formation. Both high-latitude and low-latitude processes likely contributed to forming the mid-latitude density structures, and the mid-latitude scintillation occurred at the interface of high-latitude and low-latitude forcing.

1. Introduction

While high-latitude and equatorial density irregularities and scintillations have been explored in detail, studies on mid-latitude (30°-60° magnetic latitude (MLAT)) density irregularities and scintillation are scarce, and their properties are far less understood. Statistically, radio signal scintillations are indeed much more common in the equatorial and high-latitude ionosphere, whereas those are rare in the mid-latitude ionosphere (Basu et al., 2002; Prikryl et al., 2015). Global surveys of satellite-based GPS amplitude scintillations and losses of lock suggest their occurrences are only a fraction of a percent depending on longitudes (Tsai et al., 2017; Xiong et al., 2018). Despite the low occurrence of disturbances in the mid-latitude ionosphere, a limited number of studies have shown that substantial strengths of density irregularities and scintillation occur during geomagnetically disturbed times.

Ledvina et al. (2002) gave the first report of mid-latitude amplitude scintillation during a storm, and they showed that the scintillation is associated with steep density gradients. In-situ observations of the ionosphere density found evidence of density irregularities in a mid-latitude trough during the same storm (Mishin & Blaunstein, 2008). The density irregularities in their event followed a power law with a power law index between −5/3 and −2. They suggested that instability processes such as the gradient drift instability (GDI), temperature gradient instability (TGI), and ionosphere feedback instability at the trough density gradient in the subauroral polarization stream (SAPS) region, play a role in forming the turbulence and energy cascading to smaller scales.

Density irregularities and scintillation in the mid-latitude ionosphere have also been reported in other types of density structures. Deep depletions of the F-region density have been observed during storms as structures that are separated from the main mid-latitude trough and equatorial plasma bubbles (EPBs) (Aa et al., 2018; Cherniak et al., 2019; Huang et al., 2007). Such depletions have been interpreted as EPBs rising to the plasmasphere or density structures created by the strong electric field in the SAPS region. Poleward extension of EPBs has indeed been measured as channels of airglow emission (Martinis et al., 2015). The density depletion region is associated with enhanced density irregularities similar to those in the equatorial ionosphere (Foster & Rich, 1998). The storm enhanced density (SED) plume also has steep density gradients and has been shown to be related to TEC fluctuations on a ~km scale (Heine et al., 2017).

These studies suggest that the mid-latitude ionosphere exhibits large density gradients and density irregularities during storms. However, it is not well understood how much GPS radio signals are disturbed by such density structures in the mid-latitude ionosphere. Because scintillation observations have focused on the equatorial and high latitude regions, it has been difficult to quantify impacts of mid-latitude density irregularities on scintillation. It is even more challenging to identify the distribution of scintillation against density structures over a continental scale. A large network of receivers is necessary to identify how scintillation is related to mid-latitude density structures.

In the present study, we utilize the University Navstar Consortium (UNAVCO) 1-Hz GPS receiver data in North America, and examine distributions of mid-latitude scintillation and the relation to density structures during the September 7–8, 2017 storm. This is one of the large storms in recent years, and large TEC gradients that developed in this storm have caught attention of the community (Aa et al., 2018; Jimoh et al., 2019; Li et al., 2018; Mrak et al., 2020). They showed density depletions and enhanced rate of TEC index (ROTI) in the mid-latitude ionosphere. We investigate how much such density structures impact GNSS signals and formation of density irregularities in the mid-latitude ionosphere. In addition, we compare radio signal scintillation with Super Dual Auroral Radar Network (SuperDARN) HF radar echo occurrence. SuperDARN backscatter echo locations indicate the existence of decameter-scale density irregularities in the ionosphere. Concurrent examinations of HF signal backscatters and GPS scintillation allow us to determine how ~10 m (SuperDARN), ~100 m (amplitude scintillation), and ones to tens of km (phase fluctuation) scale density irregularities are related to one another, and how such density irregularities are related to large-scale (~100s km) density structures in the mid-latitude ionosphere. Density irregularities across such a broad wavelength range have rarely been investigated, but it has been suggested that GDI and/or TGI could drive energy cascading from the km scale to the decameter scale (Eltrass et al., 2016; Prikryl et al., 2011). Our study reveals how the density irregularities at different scales are related and how they are distributed in association with large-scale density structures.

2. Data Set and Method

Data from the UNAVCO 1-Hz GPS receivers in the contiguous United States were used to obtain proxy phase (σ_{TEC}) and amplitude (SNR_4) scintillation indices (Mrak et al., 2020). The indices are defined as,

$$\sigma_{TEC} = \sqrt{\langle \left(\Delta TEC\right)^2 \rangle - \langle \Delta TEC \rangle^2} \left[TECU\right] \quad (1)$$

$$SNR_4 = \sqrt{\langle \left(\Delta SNR\right)^2 \rangle - \langle \Delta SNR \rangle^2} \left[dB\right] \quad (2)$$

where TEC is the vertical total electron content for each line-of-sight (LOS), SNR is the signal-to-noise ratio, and ΔTEC and ΔSNR are >0.1 Hz high-pass filtered TEC and SNR. The brackets compute a mean over a 1-min period of data. Satellites above 30° elevation are used to avoid multipath effects. SNR_4 represents the low-frequency component of the S_4 index. σ_{TEC} could be affected by both phase scintillation and unresolved phase variation due to the low sampling rate (Forte & Radicella, 2002; McCaffrey & Jayachandran, 2019; Wang et al., 2018). Thus σ_{TEC} is used as an indicator of phase fluctuation of the GPS signal. A similar approach was used for 1-Hz high-latitude receiver data (Ghoddousi-Fard et al., 2013).

The standard deviation of σ_{TEC} and SNR_4 was calculated as the standard deviation of the indices for each day for each receiver-satellite pair. Phase and amplitude scintillations were identified when σ_{TEC} and SNR_4 stay three times larger than the standard deviation for at least 2 min in each receiver-satellite pair. The choice of these thresholds is empirical, but as shown by Mrak et al. (2020), this threshold effectively removes instrumental noise. σ_{TEC} is similar to ROTI but has a higher time resolution.

Mrak et al. (2020) assessed a performance of the indices by comparing σ_{TEC} and SNR_4 with the standard phase and amplitude scintillation indices (σ_ϕ and S_4) that were obtained by a scintillation receiver in Texas during the September 7–8, 2017 storm. They found nearly a linear correlation between σ_{TEC} and σ_φ, and SNR_4 and S_4, indicating that σ_{TEC} and SNR_4 give similar information to the conventional scintillation indices. The scaling for this event was approximately $\sigma_\varphi \sim 6\sigma_{TEC}$, and $S_4 \sim 0.3SNR_4$. Their technical validation analysis showed a consistency between the elevated σ_{TEC} and ROTI in mid-latitude density structures. The present study will utilize the scintillation indices to conduct a more detailed investigation of the relation between the scintillation and density gradients, as well as comparisons to in-situ and SuperDARN radar observations.

The Canadian high arctic ionospheric network (CHAIN) GPS receiver network measures GPS radio signals at 50 Hz in Canada (Jayachandran et al., 2009). Four of the stations below 60° MLAT (Fort McMurray, Ministik Lake, Gillam, and Sanikiluaq) were used to measure scintillation poleward of the UNAVCO receiver coverage. σ_ϕ and S_4 were calculated from the CHAIN data.

The vertical TEC data created by the MIT Haystack Observatory (Rideout & Coster, 2006) are used to investigate TEC structures and their relation to the GPS signal scintillation. Data are gridded in $1° \times 1°$ horizontal resolution every 5 min. The five of the mid-latitude SuperDARN radars in the contiguous United States (Christmas Valley West and East, Fort Hays West and East, and Blackstone) (Nishitani et al., 2019) are used to find regions of field-aligned ionosphere density irregularities at a ~10 m size. The time resolution is 1–2 min.

The Defense Meteorological Satellite Program (DMSP) and Swarm satellites provide F-region electron density and temperature at 1 and 2 Hz, respectively. DMSP measures the topside ionosphere at ~850 km altitude, and Swarm measures regions just above the peak of the F-region ionosphere (Swarm-A/C: 450 km, Swarm-B: 510 km). In one of the Swarm passes, the 16-Hz sampling of the density measurements were available and were used to obtain a power spectrum of density irregularities.

3. Results

3.1. Latitudinal Structures

Figure 1 shows evolution of the latitudinal distribution of the ionosphere TEC, density and scintillation indices near the west and east coasts of the United States during the September 7–8, 2017 storm. North America moved from the afternoon to midnight sectors in the main and early recovery phases of the storm. Before 23:00 UT, the mid-latitude TEC was smooth and varied slowly (Figures 1b and 1i). After the sudden commencement (sharp SYM-H jump) at 23:00 UT, the SYM-H index rapidly dropped, and the mid-latitude ionospheric TEC increased abruptly on both the west and east coasts. It is known as the SED base and plume due to enhanced large-scale convection and the SAPS electric field (Foster & Rideout, 2007). The main trough can be seen as the low-TEC region that was located poleward of the SED. The enhanced TEC poleward of the main trough is the auroral oval. The region of SED and the main trough moved equatorward as the storm progressed. The equatorward boundary of the main trough is visually traced by the poleward pink dashed line.

In addition to the equatorward boundary of the trough, another major TEC gradient can be seen equatorward of the main trough, which is marked by the equatorward pink dashed line. On the east coast, the TEC between the two gradients at ~40° MLAT depleted to three TECU at 01:00 UT, as low as in the main trough. This is likely a TEC signature of the mid-latitude TEC depletion (Huang et al., 2007). In contrast, the TEC equatorward of it (~35° MLAT) was elevated to >30 TECU. In order to distinguish them clearly from the main trough and SED plume, and due to their channel-like shapes (see Section 3.2), we refer to them as

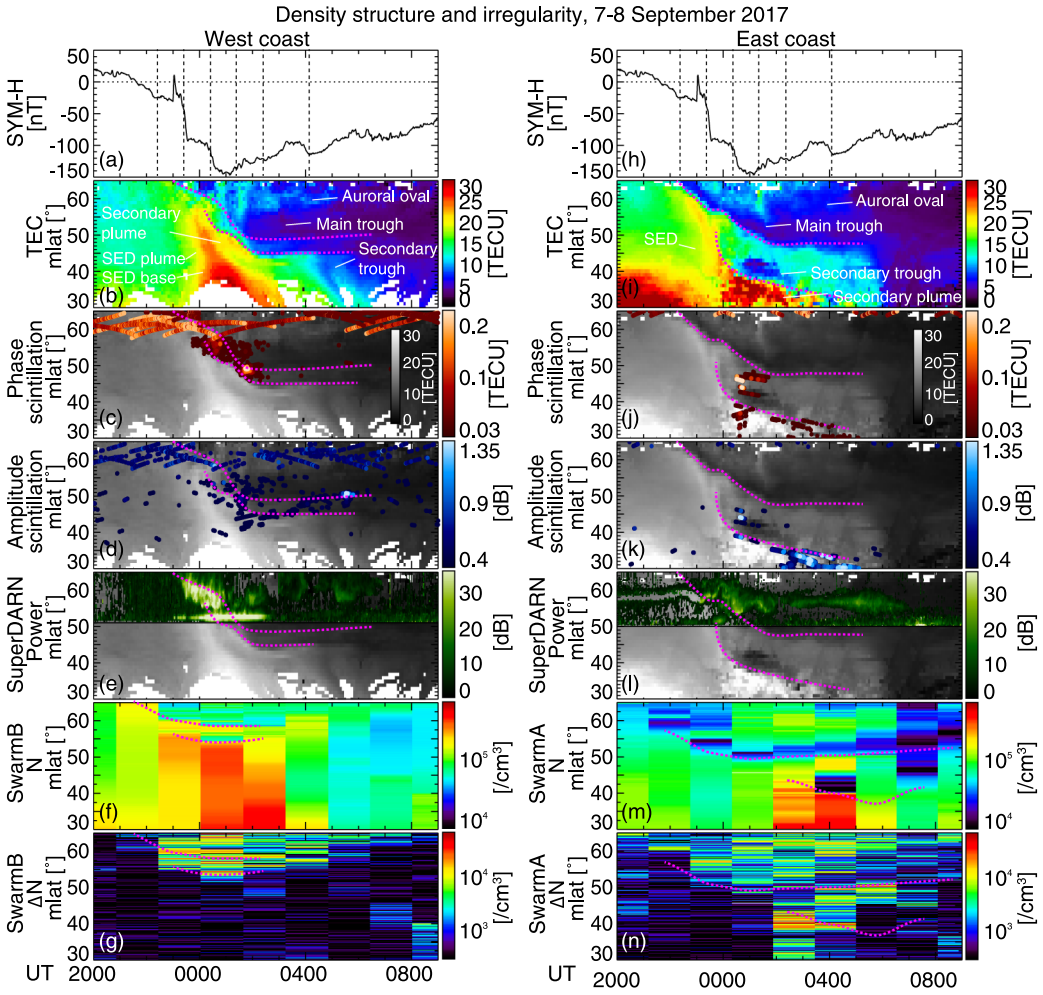

Figure 1. (a) SYM-H, (b) TEC keogram in the west coast (242° geographic longitude, MLT ~ UT – 9 h), (c), (d) σ_{TEC} and SNR_4 overlaid onto the TEC data on the grayscale, (e) SuperDARN backscatter power from the CVW radar (averaged over beam 15–23, only ionosphere echoes are used) overlaid onto the TEC data on the grayscale, (f) density along Swarm-B northern hemisphere passes, and (g) >0.1 Hz high-pass filtered Swarm-B density irregularities. The dashed lines in Panel a indicate times of images in Figure 2. The dashed pink lines visually trace major equatorward density gradients. The phase and amplitude scintillation indices are shown only where the indices are above the thresholds mentioned in Section 2 (~0.03 TECU and ~0.4 dB in most stations). The 1-Hz GPS station map can be found in Figure 3a. The format of Panels h–n is the same as Panels a–g except for the east coast (277° longitude, MLT ~ UT – 5 h), BKS SuperDARN (beam 9–17), and Swarm-A. Swarm-B and A were closest to the west and east coasts at ~0 and ~3 UT, respectively. The pierce point altitude is set to be 350 km.

a secondary trough and plume. A similar but weaker secondary trough and plume were seen on the west coast.

σ_{TEC} and SNR_4 from the receivers near each coast are overlaid onto the TEC data (gray scale) in Figures 1c, 1d, 1j and 1k. In the CHAIN receiver coverage (>57° MLAT near the east coast), the phase fluctuation was persistent, while the amplitude scintillation increased sporadically. This region corresponds to the subauroral and auroral ionosphere, where enhanced flows and precipitation likely contributed to the scintillation. In the UNAVCO receiver coverage (<57° MLAT), the enhanced scintillation indices were found primarily at the equatorward edge of the main trough, at equatorward and poleward edges of the secondary trough, and in the secondary plume. Thus, the TEC structures in the mid-latitude ionosphere were important regions for the scintillation occurrence. The region of the enhanced scintillation moved equatorward as the TEC structures moved equatorward. Enhanced σ_{TEC} and SNR_4 occurred mostly in the same region, but they did not intensify at the same time.

SuperDARN backscatter echo power from the Christmas Valley West (CVW, >51° MLAT) and Black Stone (BKS, >50° MLAT) radars is overlaid onto the TEC data in Figures 1e and 1l, respectively. The enhanced backscatter was located primarily in the main trough and around the trough equatorward boundary, and weaker radar echoes were found in the auroral oval. In the west coast, σ_{TEC}, SNR_4 and the SuperDARN echoes were almost collocated, indicating that density irregularities emerged over a broad wavelength spectrum between tens of meters and tens of kilometers. On the other hand, the scintillation indices were not elevated in the SuperDARN echo regions on the east coast. The short-range (E-region) echoes at 50°–53°MLAT were more persistent and were also enhanced in the main trough and at the TEC gradients. The E-region echoes are attributed to Farley-Buneman instability due to enhanced flows (Makarevich et al., 2015).

The last two panels of Figure 1 show the F-region density (N) and 0.1 Hz high-pass filtered density (ΔN) measured along the Swarm-B and A orbits in the northern hemisphere. Although the satellites are not fixed to the geographic longitudes, Swarm-B and A were closest to the west and east coasts at ~0 and ~03:00 UT, respectively. If the density structures are stationary, the 0.1 Hz high-pass filtering gives density structures below 80 km size down to 8 km. Consistent with the TEC data, Swarm detected two major equatorward density gradients in some of the passes, and the density gradients moved equatorward during the main phase (traced as the pink dashed lines). The troughs can be identified as the low density regions poleward of the pink dashed lines. In Swarm-B, ΔN was enhanced in the vicinity of the density gradients and in the troughs, while ΔN was small in the region equatorward of the density gradients. In Swarm-A, enhanced ΔN extended down to <30° MLAT and was most intense in the density gradient region in the early recovery phase. The occurrence regions of the density irregularities at both satellites are consistent with the occurrence regions of the enhanced scintillation indices in both coasts. $\Delta N/N$ reached ~0.2 at the density gradients in both coasts, meaning that ΔN was not a small perturbation but rather a substantial fraction of the F-region density on scales of tens of km.

3.2. Horizontal Distribution of TEC

Figure 2 shows the 2-D structure of the mid-latitude TEC during this storm at the selected times that are indicated by the dashed lines in Figure 1a. The whole sequence is given in Movie S1. Before the storm sudden commencement, the main trough was located above 60° MLAT (Figure 2a). The trough equatorward boundary is traced by the pink dashed line. During the sharp drop of the SYM-H index, the main trough rapidly moved equatorward, and the TEC equatorward of the trough increased from ~15 to ~20 TECU (Figure 2b). This is the SED base caused by enhanced electric field. A plume formed in the afternoon sector (~13–16 MLT). Then the TEC equatorward of the main trough started to form multiple gradients, with secondary troughs and plumes (Figure 2c). The TEC drop was more prominent on the east coast (at ~20 MLT). The TEC in the secondary trough became as low as the main trough, and the TEC in the secondary plume over the Gulf of Mexico became higher than the SED plume (Figures 2c and 2d). The TEC gradient between this secondary trough and plume was steeper than the gradient at the equatorward boundary of the main trough. The TEC gradients became smaller but continued to move equatorward and sunward during the early recovery phase (Figure 2e). A distortion of the TEC gradient was seen in the southwestern United States (Figure 2f).

3.3. Horizontal Distribution of Scintillation

σ_{TEC} and SNR_4 are overlaid onto the TEC maps as red and blue circles in Figure 3. The yellow crosses in Figure 3a mark the UNAVCO 1-Hz and CHAIN receiver locations. Each receiver covers a circular region of a few hundred km radius. The receivers sampled almost all parts of the contiguous United States, but the spacing is not uniform. Many of the receivers are located in the western United States, while fewer receivers exist in the eastern United States. Thus a higher density of dots in Figure 3 is not necessarily related to higher occurrence of scintillation. We focus on whether scintillation occurred or not around the receiver locations and how strong it was. There are always 4–6 GPS satellites visible at each receiver location (Figure 4), and thus multiple data points are available at each time around each station.

σ_{TEC} and SNR_4 at mid-latitudes were mostly below the threshold (thus not shown) in the early main phase (Figures 3a and 3b), while σ_{TEC} and SNR_4 above 60° MLAT were already elevated. As the trough moved

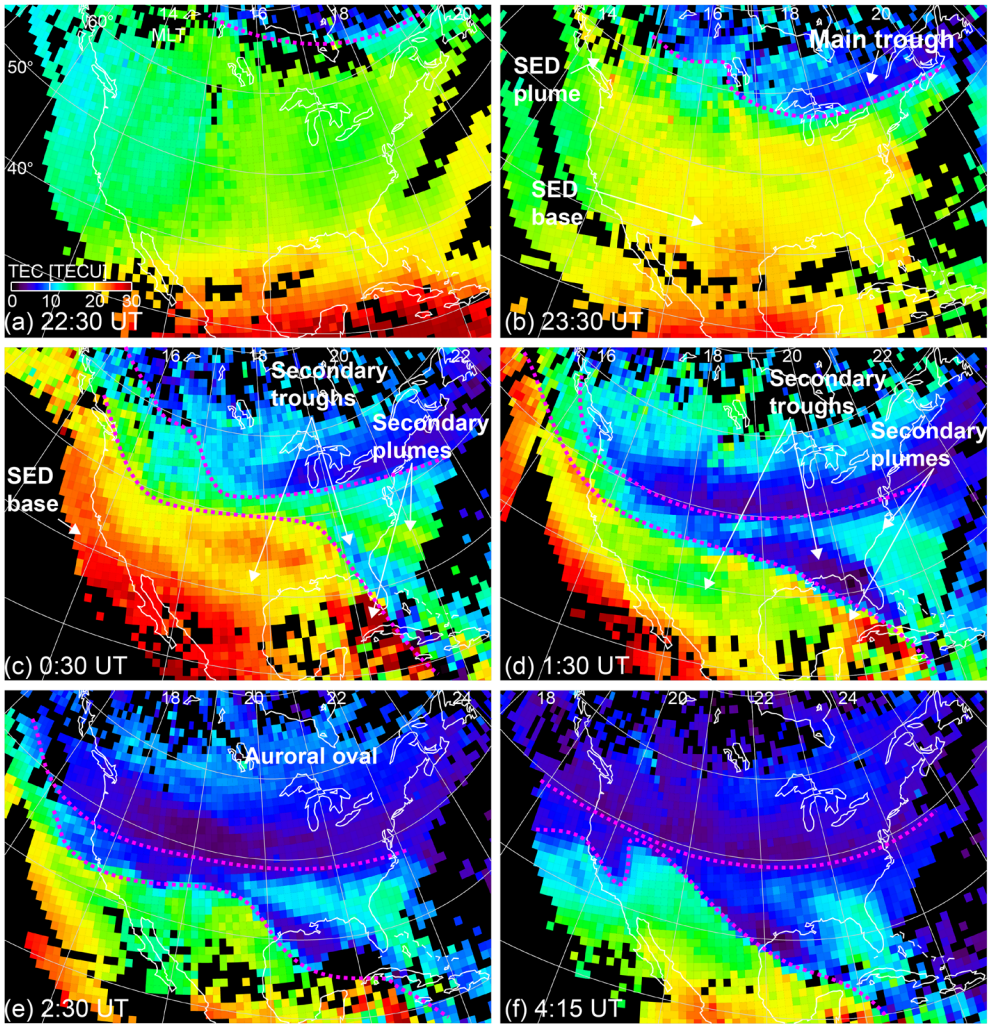

Figure 2. Selected images of TEC maps. The dashed pink lines visually trace major equatorward density gradients. The whole sequence is given in Movie S1.

equatorward (Figure 3c), σ_{TEC} and SNR_4 started to increase in the TEC gradient region equatorward of the main trough in the west coast. About 2 meters of GPS positioning error have been reported in the region of scintillation (Yang et al., 2020), and thus the measured level of scintillation significantly impacts the GPS signal. In the east coast, the secondary trough and plume developed, and σ_{TEC} and SNR_4 were enhanced within and at the boundary of the secondary trough. Enhanced σ_{TEC} and SNR_4 at mid-latitudes were found in the northwestern United States, while σ_{TEC} and SNR_4 were not elevated in the midwestern United States at that time even though receivers were present. The enhanced σ_{TEC} and SNR_4 then extended to wider longitudes in the TEC gradient regions (Figure 3d). σ_{TEC} and SNR_4 became weaker in the recovery phase but can still be seen in limited regions in the vicinity of the TEC gradients (Figures 3e and 3f).

Figure 4 shows a time-series of 1-Hz GPS receiver data from two of the stations shown in Figure 3a (Hopedale, IL [HDIL], 40.6° latitude and 271° longitude in geographic and Wichita Mountain, OK (WMOK), 34.7° latitude and 261° longitude). Consistent with the TEC data in Figure 2, TEC at each LOS was smooth and slowly varying before 23:00 UT. At 23:00–01:30 UT, TEC increased and then decreased with multiple excursions. The first TEC enhancement corresponds to the SED base. The subsequent reductions and enhancements occurred at the TEC gradients identified in Figure 2 and are substructures at the TEC gradients including the secondary trough and plume. After 01:30 UT, HDIL went into the main trough, and WMOK stayed in the secondary plume.

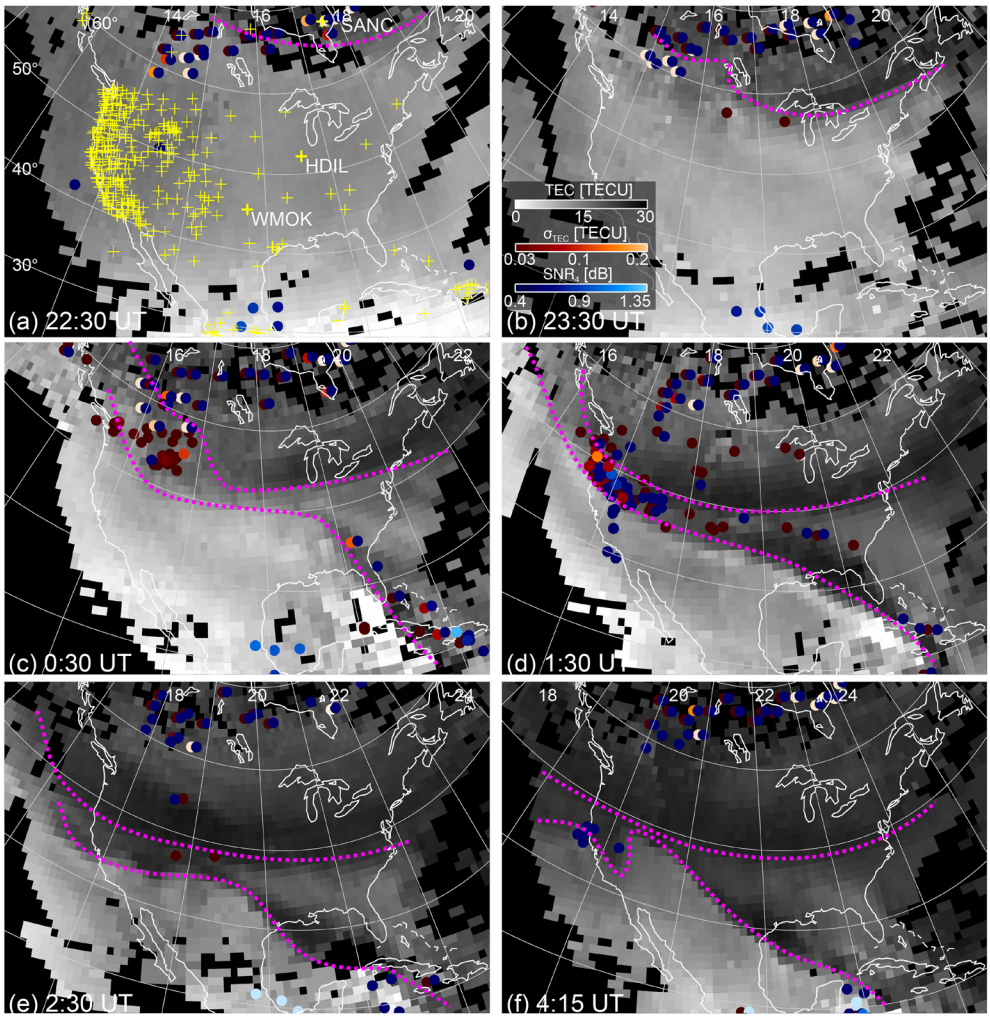

Figure 3. σ_{TEC} (red) and SNR_4 (blue) from the UNAVCO 1-Hz and CHAIN receiver data overlaid onto the TEC maps in the gray scale. The yellow crosses in Panel a show locations of the receivers.

The TEC variations at 23:00–01:30 UT did not occur simultaneously at the two receivers, but were measured first at HDIL and then WMOK. At each receiver, the GPS satellites to the north of the receivers (±90° azimuth) detected the TEC variations first, and the satellites to the south of the receivers (180° ± 90° azimuth) observed them later. It supports the interpretation that the TEC structures mentioned above were primarily spatial structures that were oriented azimuthally and moved equatorward.

Enhanced σ_{TEC} and SNR_4 were detected at ~23:00–04:00 UT and were associated with these mid-latitude TEC gradients. The largest σ_{TEC} and SNR_4 were seen at the sharp TEC gradients at 00:00–02:00 UT, when the steepest TEC gradients marked in Figure 2 passed over the HDIL and WMOK receivers. The amplitude and timing of scintillation varied differently for different GPS satellites, indicating that the enhanced scintillation is not due to instrumental noise but rather is a signal disturbance originating in the ionosphere. σ_{TEC} and ROTI showed essentially the same variations, meaning that the two indices are nearly identical, although σ_{TEC} highlights faster variations.

The existence of enhanced σ_{TEC} and SNR_4 in the mid-latitude TEC gradients indicates that density irregularities were present at the trough equatorward boundary and the secondary trough and plume. While it is ambiguous if the enhanced σ_{TEC} arose from scintillation due to km-scale density irregularities or phase variations due to drifting density structures, the enhanced SNR_4 provides evidence of scintillation by hundreds

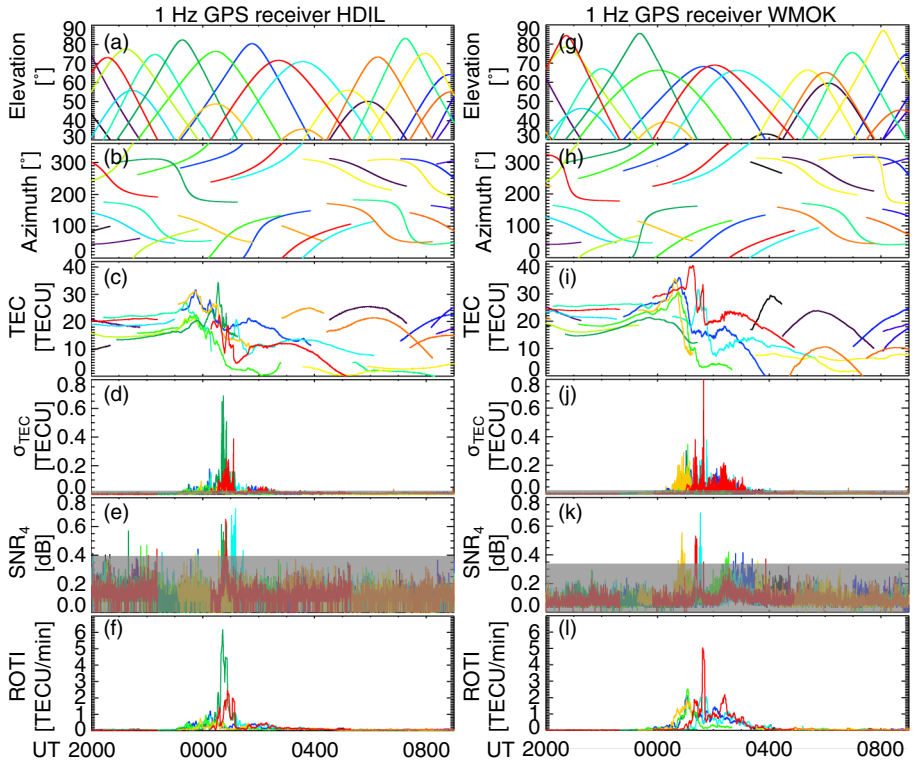

Figure 4. Time series of 1-Hz GPS receiver data at HDIL and WMOK. (a), (g) Satellite elevation angle, (b), (h) azimuth angle, (c), (i) TEC, (d), (j) σ_{TEC}, (e), (k) SNR_4, and (f), (l) ROTI. The colors indicate different GPS satellites. The gray regions mask data less than 3 times the standard deviation of the signal, which are not used. The receiver locations are marked in Figure 3a. The whole sequence is given in Movie S2.

of meter density irregularities. The density irregularities developed when the TEC gradients formed and moved equatorward during the storm main phase, and weakened as the storm recovered.

3.4. Horizontal Distribution of SuperDARN Echoes

To find location of decameter-scale density irregularities, the echo power measured by the mid-latitude SuperDARN radars is overlaid onto the TEC maps in Figure 5. The radar coverage is limited to regions above ~50° MLAT, and thus we focus on a comparison to the TEC and scintillation indices above 50° MLAT. Only ionospheric echoes were used and ground scatter was removed. Before 23:00 UT, echo backscatter was weak and was limited to the main trough (Figure 5a). As the storm progressed, the echo power increased substantially and spread over the TEC gradient region and in the main trough (Figures 5b and 5c). Later, the radars no longer covered the TEC gradient region, but echoes were found in the main trough and auroral oval (Figure 5d). The echoes weakened as the storm proceeded to the recovery phase.

The association between the radar echoes and TEC gradients indicates that decameter-scale density irregularities were developed at the trough equatorward boundary and secondary plume. In the northwest United States, the radar echoes were collocated with the enhanced σ_{TEC} and SNR_4 as in Figure 3c, and thus a wide wavelength range of density irregularities (tens of m to tens of km) were present at the mid-latitude TEC gradients. In contrast, the radar echoes extended to all longitudes as in Figure 5c, but the enhanced σ_{TEC} and SNR_4 were not seen in the midwestern and northeast United States at that time. It suggests that the density irregularities at different scales do not always appear at the same time and place but depend on local plasma conditions.

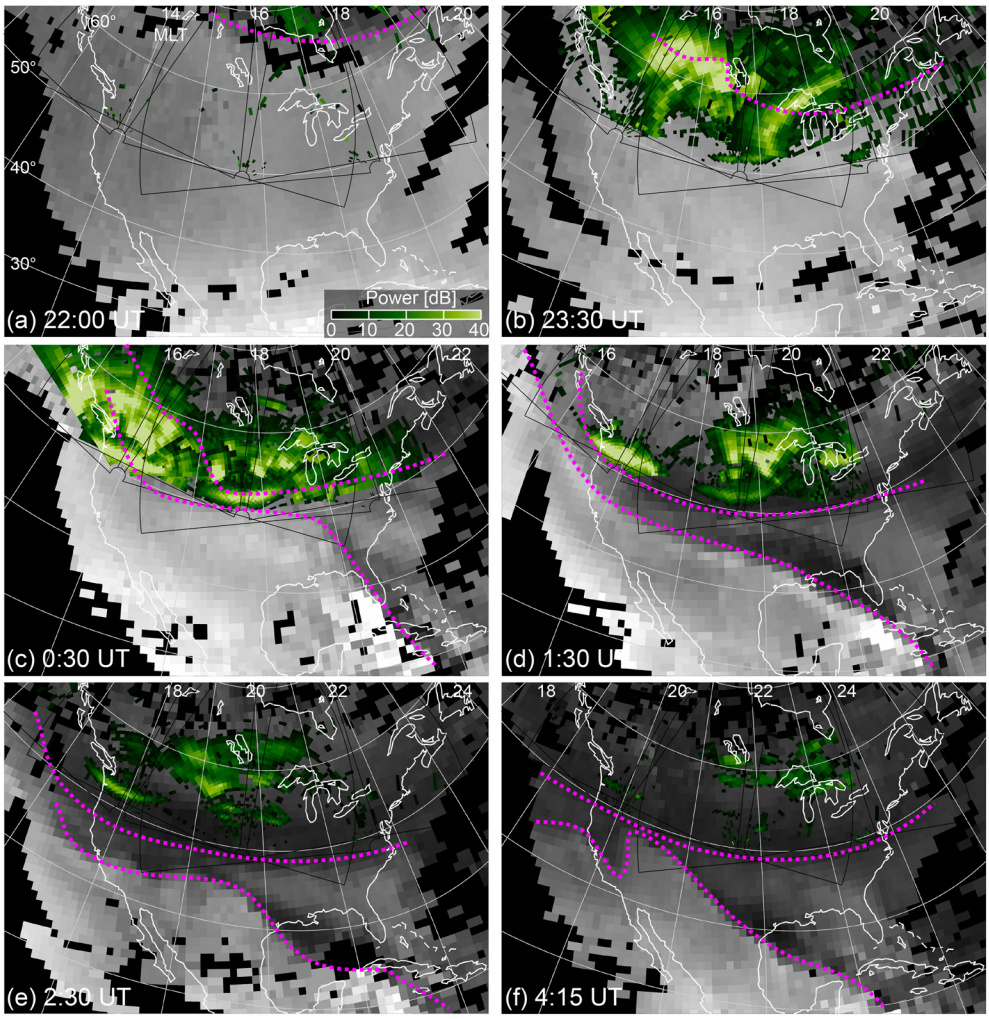

Figure 5. Echo power from the mid-latitude SuperDARN radars in North America overlaid onto the TEC maps. The black lines depict the fields-of-view of the SuperDARN radars.The whole sequence is given in Movie S3.

3.5. DMSP and Swarm Conjunctions

Here we show DMSP and Swarm observations of ionospheric density to examine how the ground-based TEC, TEC gradients and density irregularity correspond to in-situ density structures. Figures 6 and 7 show eight selected satellite passes over North America during this event. Orbits in the southern hemisphere were mapped to the northern hemisphere using the Tsyganenko (2002) magnetic field model. Although density structures in the southern hemisphere may be different from the northern hemisphere, seasonal effects will be small because of the event in equinox, and as shown below, structures of the in-situ density in the southern hemisphere and TEC in the northern hemisphere overall agree well.

During the storm main phase around 00:00 UT (Figures 6a–6f), DMSP-18 and Swarm-B measured density peaks just equatorward of the main trough (~55° MLAT) in agreement with the mid-latitude TEC at the SED base. The high-pass filtered density shows density irregularities in the SED base and main trough. $\Delta N/N$ was about 3% (DMSP-18) and 10% (Swarm-B). The SED base density corresponded to enhanced sunward flows (likely SAPS) much more pronounced than upward flows (Figure 6d, no data after 00:20 UT), indicating that the enhanced density in this region was transported from later MLT. Swarm-B detected another density enhancement and density fluctuation around −60° MLAT. It is in the auroral oval and is not discussed in this study.

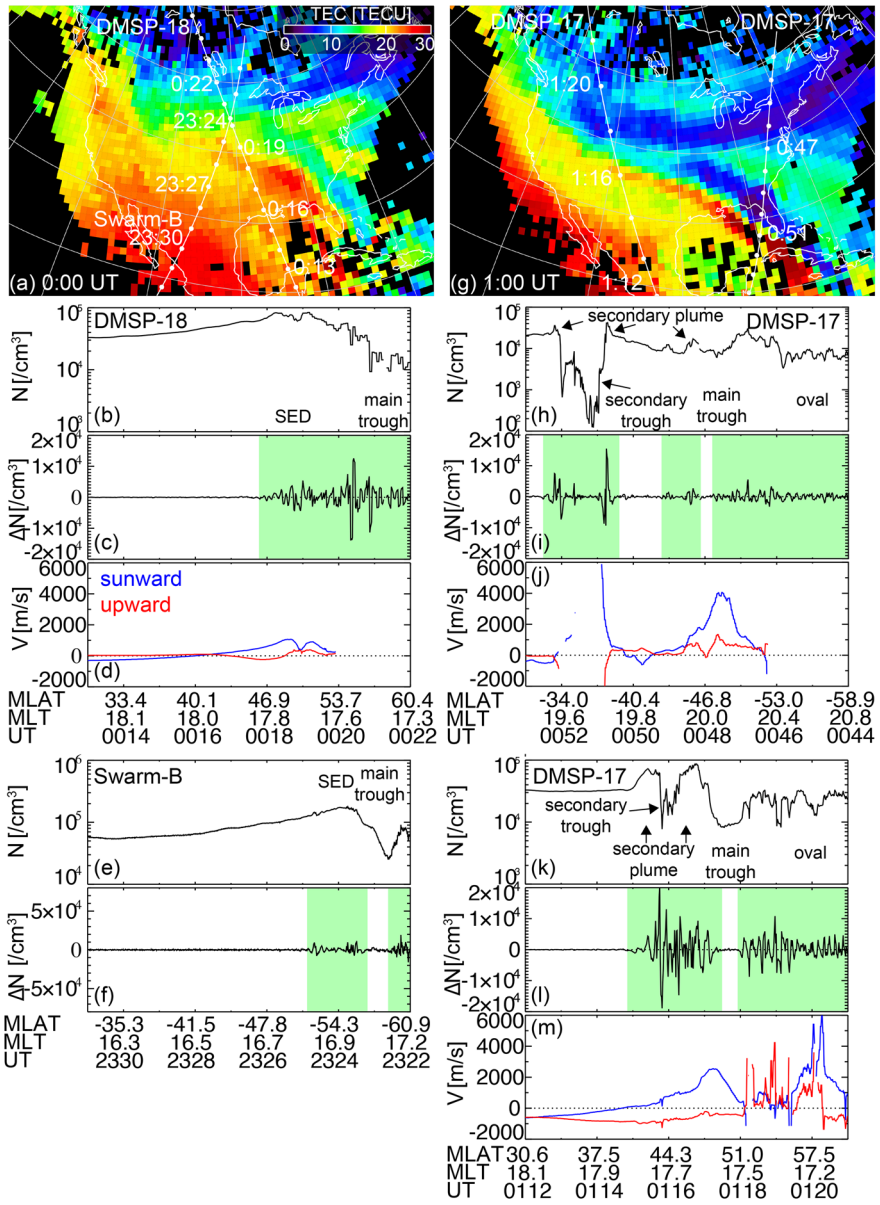

Figure 6. (a), (g) TEC maps at 0:00 and 1:00 UT. The solid lines mark the satellite tracks. (b, e, h, k) Density, and (c), (i), (f), (l) >0.1 Hz high-pass filtered density measured by DMSP and Swarm. (d, j, m) Cross-track drift velocity by DMSP. The green shades in the high-pass filtered density panels indicate the regions of enhanced density irregularities. None of the Swarm passes had drift measurements in this time event.

When DMSP-17 passed the center of the secondary trough in the east coast (00:51–00:52 UT, Figures 6h–6j), the satellite detected a steep density drop by two orders of magnitude. This is an unusually low density in the duskside mid-latitude ionosphere, and it corresponds to the secondary trough. The density enhancements at other latitudes are the secondary plumes, and they are more structured than seen in TEC. Although the velocity measurements were limited, the drift was suggested to be strongly sunward and downward in the secondary trough. The sunward velocity is consistent with the azimuthal elongation of the density depletion, and the downward velocity would indicate a downflow from higher altitudes including field-aligned transport from lower latitudes.

At 01:15–01:18 UT (Figures 6k–6m), DMSP-17 detected two secondary plumes and a secondary trough in between. They were located in enhanced sunward flow regions. The secondary plumes and trough had

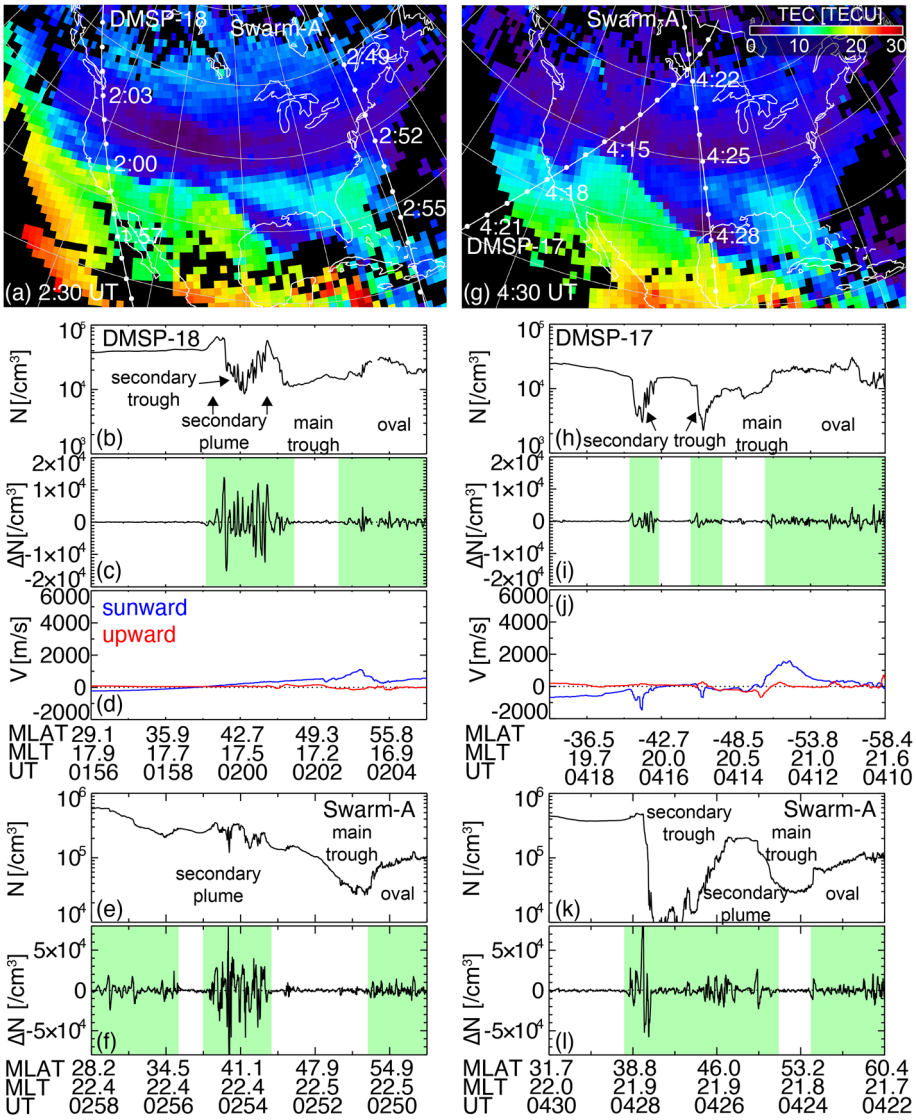

Figure 7. TEC maps at 2:30 and 4:30 UT, and four DMSP and Swarm satellite data. The format is the same as in Figure 6.

pronounced density irregularities that are comparable to the irregularities in the auroral oval. $\Delta N/N$ at the DMSP altitude increased to ~12% at mid latitudes, and became larger than the irregularities in the auroral oval. In contrast, the main trough did not have substantial density irregularities.

Essentially the same density structures and irregularities were observed when DMSP-18 passed the same region in the west coast about 1 h later (Figures 7a–7d). Thus the density structures were quasi-steady and slowly varying over time, and the density irregularities were persistent at the density gradients. Swarm-A passed the secondary plume on the east coast (Figures 7e and 7f), and detected enhanced density irregularities ($\Delta N/N \sim 10\%$) that extended over a wide latitude range (30°–45° MLAT).

DMSP-17 detected the main (04:13 UT) and secondary (04:14–04:17 UT) troughs on the west coast in the early recovery phase (Figures 7g–7j). The two secondary troughs along the satellite orbit correspond to a single trough but with a distortion of the density gradient. Anti-sunward flow enhancements were associated with the density depletions. The density irregularities were still present but became smaller. However, its relative magnitude became larger as the trough deepened ($\Delta N/N \sim 50\%$). The secondary trough was deeper and broader along the Swarm-A orbit, with pronounced density irregularities (Figures 7k and 7l).

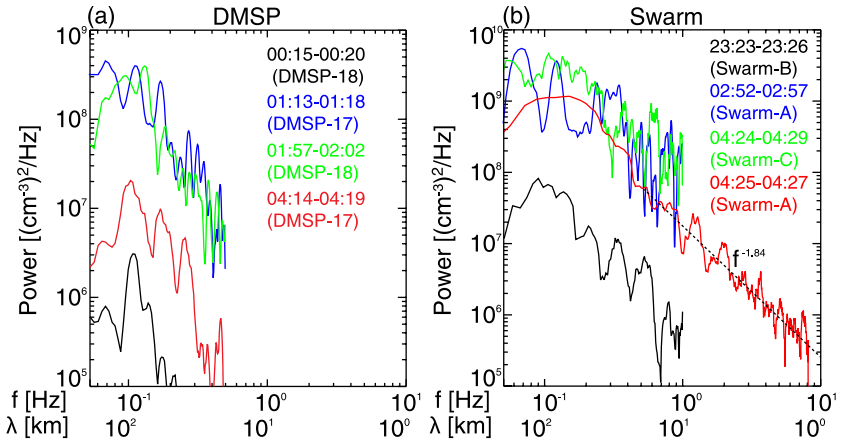

Figure 8. Power spectra of the DMSP and Swarm density shown in Figures 6 and 7 at time windows specified in the panels. The dashed lines show power-law fits to data above 0.6 Hz.

The in-situ density irregularities at mid-latitudes were primarily seen at the SED base, secondary plume and trough, and the equatorward boundary of the main trough. It is consistent with the locations of the enhanced scintillation and SuperDARN echoes seen in Figures 3 and 5, suggesting that the in-situ irregularities are (at least part of) the source of the scintillations. The density irregularities are also located in the region of enhanced flows, and thus density irregularities passing across the ray path of the GPS signal would also contribute to the phase variation of the radio signal.

We also calculated power spectra of the density where the mid-latitude density irregularities were seen in Figures 6 and 7. The horizontal axis in Figure 8 also shows the wavelength along the satellite orbits assuming that the measured density structures are quasi-stationary. The plasma velocity along the satellite orbits is not known and thus the wavelength scale is only given for a reference. At both the DMSP and Swarm satellite locations, the density irregularities were amplified by 1–2 orders of magnitude at all frequencies/wavelengths as the storm developed in the main phase (from the black to blue and green orbits). Then the irregularities weakened during the recovery phase (red). Swarm-A had 16-Hz density observations in the secondary plume at 04:25–04:27 UT, and we can see a power-law spectrum at 0.5–8 Hz (or ~1–15 km size if stationary). The presence of the power-law spectrum suggests that the density irregularities are related to turbulence developed in the secondary plume. The ~ −1.8 spectral slope has also been seen in the high-latitude ionosphere (Mounir et al., 1991) and is characteristic to predicted spectra for the gradient drift instability (GDI) (Gondarenko & Guzdar, 2004). This slope suggests that GDI at the density gradients in the mid-latitude ionosphere is responsible for forming the density irregularities.

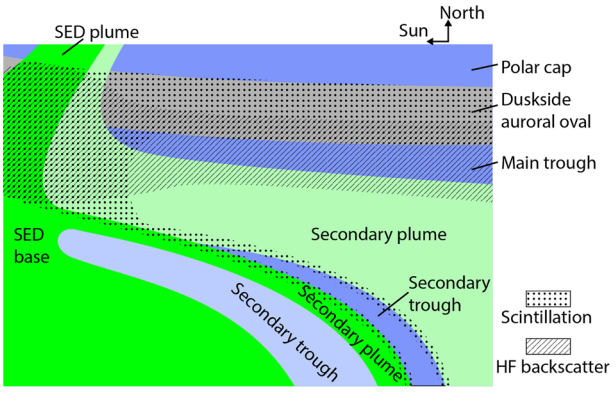

Figure 9. Schematic illustration of the density structures and occurrence regions of the scintillation and HF backscatters in the afternoon-dusk sector during the main phase. The green colors indicate high density regions, and the blue colors indicate low density regions. The noon is to the left and the pole is to the top. The regions of dots and oblique lines indicate the scintillation and HF backscatter occurrence regions.

4. Conclusion

We investigated the 2-D distribution of mid-latitude GPS radio signal scintillation in North America during the September 7–8, 2017 storm. By taking advantage of the continental-scale coverage of the 1-Hz UNAVCO GPS receivers, we were able to identify how mid-latitude scintillation is related to large-scale and local TEC structures in the afternoon-to-midnight sector. Key density structures and occurrence regions of the scintillation and HF backscatter are illustrated in Figure 9. Both phase and amplitude scintillations intensified during the storm main and early recovery phases in TEC gradients in the mid-latitude ionosphere, which were identified to be the SED base, equatorward boundary of the main trough, secondary trough and secondary plume. Scintillation was also found in the main trough but the magnitude was smaller. The SuperDARN backscatter

echoes were also enhanced in the TEC gradient region and in the main trough, indicating that density irregularities emerged over a broad wavelength spectrum between tens of meters and tens of kilometers.

The main trough, trough equatorward boundary and part of the secondary plumes and troughs moved equatorward from ~60° to ~40° MLAT as the storm developed. The secondary plume and trough near the east coast were located more equatorward and extended to the low-latitude ionosphere. The TEC structures and scintillation at mid-latitudes in this storm are affected by both high-latitude and low-latitude processes and the mid-latitude ionosphere is an interface of both processes.

The scintillation was not uniformly distributed in the TEC gradient regions but had longitudinal dependence. The scintillation preferentially occurred where the TEC gradients were most pronounced at the trough equatorward boundary near the west coast and at the boundary between the secondary plume and trough near the east coast. The SuperDARN echoes were also the strongest near the west coast, although weaker echoes were distributed over the entire TEC gradient region within the radar field-of-view. In addition, the TEC gradients at those locations were tilted away from the north-south directions. We suggest that the large density gradients and orientation affect where density irregularities and scintillation develop.

The mid-latitude TEC gradients coincided with the in-situ density gradients at both Swarm and DMSP altitudes, supporting that the density structures inferred from the TEC maps are primarily horizontal density structures. The mid-latitude scintillation was closely related to the density irregularities in the in-situ density gradient regions during the storm main and early recovery phases. The density irregularity amplitude reached ~10%–50% of the background density, and thus the irregularities significantly disturb the background density structures. The density power spectrum showed a ~−1.8 spectral slope, consistent with the theoretical expectation of the GDI. Growth and cascades of density structures at the density gradients under the storm-time convection and flow channels likely contributed to forming the density irregularities that caused the scintillation.

Data Availability Statement

Swarm is a European Space Agency mission; provision of data used in this study was also supported by the Canadian Space Agency. The GPS TEC, UNAVCO, CHAIN, TEC, SuperDARN, DMSP and Swarm data were obtained through www.unavco.org, chain.physics.unb.ca, cedar.openmadrigal.org, vt.superdarn.org and swarm-diss.eo.esa.int, respectively.

Acknowledgments
This work was supported by NASA grant 80NSSC18K0657, 80NSSC20K0604 and 80NSSC20K0725, NSF grant AGS-1907698, and AFOSR grant FA9559-16-1-0364. We thank the NASA Living With a Star Institute program on "Space Weather Impacts on GNSS Radio Occultations at Mid-Latitudes," CEDAR for the "Grand Challenge: Multi scale I-T system dynamics" workshop, NASA HERMES DRIVE Center, and ISSI for the "Multi-Scale Magnetosphere-Ionosphere-Thermosphere Interaction" workshop.

References

Aa, E., Huang, W., Liu, S., Ridley, A., Zou, S., Shi, L., et al. (2018). Midlatitude plasma bubbles over China and adjacent areas during a magnetic storm on 8 September 2017. *Space Weather*, *16*, 321–331. https://doi.org/10.1002/2017SW001776

Basu, S., Groves, K. M., Basu, S., & Sultan, P. J. (2002). Specification and forecasting of scintillations in communication/navigation links: Current status and future plans. *Journal of Atmospheric and Solar-Terrestrial Physics*, *64*(16), 1745–1754. https://doi.org/10.1016/s1364-6826(02)00124-4

Cherniak, I., Zakharenkova, I., & Sokolovsky, S. (2019). Multi-instrumental observation of storm-induced ionospheric plasma bubbles at equatorial and middle latitudes. *Journal of Geophysical Research: Space Physics*, *124*, 1491–1508. https://doi.org/10.1029/2018JA026309

Eltrass, A., Scales, W. A., Erickson, P. J., Ruohoniemi, J. M., & Baker, J. B. H. (2016). Investigation of the role of plasma wave cascading processes in the formation of midlatitude irregularities utilizing GPS and radar observations. *Radio Science*, *51*, 836–851. https://doi.org/10.1002/2015RS005790

Forte, B., & Radicella, S. M. (2002). Problems in data treatment for ionospheric scintillation measurements. *Radio Science*, *37*(6), 1096. https://doi.org/10.1029/2001RS002508

Foster, J. C., & Rich, F. J. (1998). Prompt midlatitude electric field effects during severe geomagnetic storms. *Journal of Geophysical Research*, *103*(A11), 26367–26372. https://doi.org/10.1029/97JA03057

Foster, J. C., & Rideout, W. (2007). Storm enhanced density: Magnetic conjugacy effects. *Annales Geophysicae*, *25*, 1791–1799.

Ghoddousi-Fard, R., Prikryl, P., & Lahaye, F. (2013). GPS phase difference variation statistics: A comparison between phase scintillation index and proxy indices. *Advances in Space Research*, *52*(8), 1397–1405. https://doi.org/10.1016/j.asr.2013.06.035

Gondarenko, N. A., & Guzdar, P. N. (2004). Density and electric field fluctuations associated with the gradient drift instability in the high-latitude ionosphere. *Geophysical Research Letters*, *31*, L11802. https://doi.org/10.1029/2004GL019703

Heine, T. R. P., Moldwin, M. B., & Zou, S. (2017). Small-scale structure of the midlatitude storm enhanced density plume during the 17 March 2015 St. Patrick's Day storm. *Journal of Geophysical Research: Space Research*, *122*, 3665–3677. https://doi.org/10.1002/2016JA022965

Huang, C.-S., Foster, J. C., & Sahai, Y. (2007). Significant depletions of the ionospheric plasma density at middle latitudes: A possible signature of equatorial spread F bubbles near the plasmapause. *Journal of Geophysical Research*, *112*, A05315. https://doi.org/10.1029/2007JA012307

Jayachandran, P. T., Langley, R. B., MacDougall, J. W., Mushini, S. C., Pokhotelov, D., Hamza, A. M., et al. (2009). Canadian high Arctic ionospheric network (CHAIN). *Radio Science*, *44*, RS0A03. https://doi.org/10.1029/2008RS004046

Jimoh, O., Lei, J., Zhong, J., Owolabi, C., Luan, X., & Dou, X. (2019). Topside ionospheric conditions during the 7–8 September 2017 geomagnetic storm. *Journal of Geophysical Research: Space Physics*, *124*, 9381–9404. https://doi.org/10.1029/2019ja026590

Ledvina, B. M., Makela, J. J., & Kintner, P. M. (2002). First observations of intense GPS L1 amplitude scintillations at midlatitude. *Geophysical Research Letters*, *29*(14). https://doi.org/10.1029/2002GL014770

Li, G., Ning, B., Wang, C., Abdu, M. A., Otsuka, Y., Yamamoto, M., et al. (2018). Storm-enhanced development of postsunset equatorial plasma bubbles around the meridian 120°E/60°W on 7–8 September 2017. *Journal of Geophysical Research: Space Physics*, *123*, 7985–7998. https://doi.org/10.1029/2018JA025871

Makarevich, R. A., Forsythe, V. V., & Kellerman, A. C. (2015). Electric field control of *E* region coherent echoes: Evidence from radar observations at the South Pole. *Journal of Geophysical Research: Space Research*, *120*, 2148–2165. https://doi.org/10.1002/2014JA020844

Martinis, C., Baumgardner, J., Mendillo, M., Wroten, J., Coster, A., & Paxton, L. (2015). The night when the auroral and equatorial ionospheres converged. *Journal of Geophysical Research: Space Research*, *120*, 8085–8095. https://doi.org/10.1002/2015JA021555

McCaffrey, A. M., & Jayachandran, P. T. (2019). Determination of the refractive contribution to GPS phase "scintillation". *Journal of Geophysical Research: Space Physics*, *124*, 1454–1469. https://doi.org/10.1029/2018JA025759

Mishin, E., & Blaunstein, N. (2008). Irregularities within Subauroral Polarization Stream-Related Troughs and GPS Radio Interference at Midlatitudes. In P. M. Kintner, A. J. Coster, T. Fuller-Rowell, A. J. Mannucci, M. Mendillo, & R. Heelis, (Eds.), *Midlatitude ionospheric dynamics and disturbances* (pp. 291–295). https://doi.org/10.1029/181GM26

Mounir, H., Cerisier, J. C., Berthelier, A., Lagoutte, D., & Beghin, B. (1991). The small-scale turbulent structure of the high latitude ionosphere: ARCAD-AUREOL-3 observations. *Annales Geophysicae*, *9*, 725–737.

Mrak, S., Semeter, J., Nishimura, Y., Rodrigues, F. S., Coster, A. J., & Groves, K. (2020). Leveraging geodetic GPS receivers for ionospheric scintillation science. *Radio Science*, *55*, e2020RS007131. https://doi.org/10.1029/2020rs007131

Nishitani, N., Ruohoniemi, J. M., Lester, M., Baker, J. B. H., Koustov, A. V., Shepherd, S. G., et al. (2019). Review of the accomplishments of mid-latitude Super Dual Auroral Radar Network (SuperDARN) HF radars. *Progress in Earth and Planetary Science*, *6*(1), 27. https://doi.org/10.1186/s40645-019-0270-5

Prikryl, P., Jayachandran, P. T., Chadwick, R., & Chadwick, R. (2011). Climatology of GPS phase scintillation and HF radar backscatter for the high-latitude ionosphere under solar minimum conditions. *Annales Geophysicae*, *29*, 377–392. https://doi.org/10.5194/angeo-29-377-2011

Prikryl, P., Jayachandran, P. T., Chadwick, R., & Kelly, T. D. (2015). Climatology of GPS phase scintillation at northern high latitudes for the period from 2008 to 2013. *Annals of Geophysics-Germany*, *33*(5), 531–545. https://doi.org/10.5194/angeo-33-531-2015

Rideout, W., & Coster, A. (2006). Automated GPS processing for global total electron content data. *GPS Solutions*, *10*, 219–228. https://doi.org/10.1007/s10291-006-0029-5

Tsai, L., Su, S.-Y., & Liu, C.-H. (2017). Chao-Han LiuGlobal morphology of ionospheric F-layer scintillations using FS3/COSMIC GPS radio occultation data. *GPS Solutions*, *21*(3), 1037–1048. https://doi.org/10.1007/s10291-016-0591-4

Tsyganenko, N. A. (2002). A model of the magnetosphere with a dawn-dusk asymmetry, 1, Mathematical structure. *Journal of Geophysical Research*, *107*(A8). https://doi.org/10.1029/2001JA000219

Wang, Y., Zhang, Q.-H., Jayachandran, P. T., Moen, J., Xing, Z.-Y., Chadwick, R., et al. (2018). Experimental evidence on the dependence of the standard GPS phase scintillation index on the ionospheric plasma drift around noon sector of the polar ionosphere. *Journal of Geophysical Research: Space Physics*, *123*, 2370–2378. https://doi.org/10.1002/2017JA024805

Xiong, C., Stolle, C., & Park, J. (2018). Climatology of GPS signal loss observed by Swarm satellites. *Annales Geophysicae*, *36*, 679–693. https://doi.org/10.5194/angeo-36-679-2018

Yang, Z., Mrak, S., & Morton, Y. J. (2020). Geomagnetic storm induced mid-latitude ionospheric plasma irregularities and their implications for GPS positioning over North America: A case study. In *2020 IEEE/ION position, location and navigation symposium (PLANS)*. IEEE. (pp. 234–238).